Journal of Applied Physics

RESEARCH ARTICLE | JUNE 11 2024

Carrier transport simulation methods for electronic devices with coexistence of quantum transport and diffusive transport

Liang Tian ; Wei E. I. Sha ; Hao Xie; Dongxue Liu; Tian-Ge Sun; Yin-Shui Xia ; Wenchao Chen

J. Appl. Phys. 135, 225703 (2024)
https://doi.org/10.1063/5.0209479

Journal of Applied Physics ARTICLE pubs.aip.org/aip/jap

Carrier transport simulation methods for electronic devices with coexistence of quantum transport and diffusive transport

Cite as: J. Appl. Phys. **135**, 225703 (2024); doi: 10.1063/5.0209479
Submitted: 21 March 2024 · Accepted: 23 May 2024 ·
Published Online: 11 June 2024

Liang Tian,[1,2] Wei E. I. Sha,[2,a)] Hao Xie,[3] Dongxue Liu,[4] Tian-Ge Sun,[4] Yin-Shui Xia,[5] and Wenchao Chen[1,2,a)]

AFFILIATIONS

[1]ZJU-UIUC Institute, International Campus, Zhejiang University, Haining 314400, China
[2]Innovative Institute of Electromagnetic Information and Electronic Integration, College of Information and Electronic Engineering, Zhejiang University, Hangzhou 310058, China
[3]School of Information and Electrical Engineering, Hangzhou City University, Hangzhou 310015, China
[4]Science and Technology Research Institute, China Three Gorges Corporation, 2 Liangshi Street, Tongzhou District, Beijing, 101199, China
[5]Faculty of Electrical Engineering and Computer Science, Ningbo University, Ningbo 315211, China

[a)]**Authors to whom correspondence should be addressed:** wenchaochen@zju.edu.cn and weisha@zju.edu.cn

ABSTRACT

In this manuscript, carrier transport simulation methods are proposed for devices with the coexistence of quantum transport and diffusive transport by combining the nonequilibrium Green's function method with the drift-diffusion transport simulation method. Current continuity between quantum transport and drift-diffusion transport is ensured by setting quantum transport current as the connection boundary condition of drift-diffusion simulation or by introducing quantum transport-induced carrier generation rates to drift-diffusion simulation. A comprehensive study of our method and the method combining the Wentzel–Kramers–Brillouin (WKB) method with the drift-diffusion transport simulation method is performed for n-type tunnel oxide passivating contact solar cell to investigate their applicable conditions and balance the accuracy and computational cost. As the oxide barrier width, barrier height, and electron effective mass increase, or the doping concentration in the electron transport layer decreases to the extent that the blocking effect of the oxide barrier on light-generated electrons becomes significant, method I is more accurate since the transmission coefficient near the conduction band edge calculated by WKB is overestimated; otherwise, method II is more suitable due to its low computational cost without the loss of accuracy. In addition, the differences between current densities, carrier densities, and Shockley–Read–Hall recombination rates simulated under the two current continuity conditions for the solar cell with different carrier mobilities are also further explored and analyzed.

I. INTRODUCTION

Scientists introduce nanoscale structures into macroscopic devices to enhance their performance, thus leading to the coexistence of quantum effects and diffusive carrier transport as shown in Fig. 1. For example, a nanometer scale surface passivated oxide that carriers can tunnel through is introduced to the solar cell to reduce the surface recombination loss and, hence, increase its efficiency; the solar cell is named tunnel oxide passivating contact (TOPCon) solar cell.[1–3] Quantum wells are introduced into solar cells to enhance light absorption at long wavelengths[4,5] because their bandgap can be tuned by varying the width. A quantum well

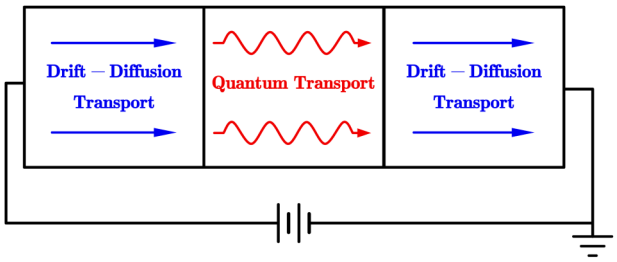

FIG. 1. Schematic of devices with the coexistence of quantum transport and diffusive transport.

is introduced to heterojunctions to fabricate the resonant tunneling diode,[6,7] which is capable of ultrahigh-speed operation and can be used as terahertz oscillators and terahertz emitters.[8]

Simulation methods have been proposed to deal with carrier transport in various semiconductor devices with different scales. The nonequilibrium Green's function (NEGF) method widely used for nanoscale devices[9–14] provides a rigorous framework to deal with quantum transport. Diffusive transport can be simulated by solving drift-diffusion transport equations by the finite element method (FEM) or finite difference (FD) method.[15–19] In addition, scholars are also dedicated to incorporating quantum effects into drift-diffusion simulation.[20–22] The density gradient confinement model is proposed by introducing a quantum potential gradient term to capture the quantum confinement effect on drift-diffusion transport.[20,21] A tunneling-induced carrier generation term is introduced to diffusive transport equations to account for carrier tunneling through the Schottky barrier.[22]

Typically, people introduce a tunneling-induced carrier generation term calculated by the Wentzel–Kramers–Brillouin (WKB) approximation method into the drift-diffusion transport equations to simulate devices with the coexistence of quantum transport and diffusive transport.[23–26] However, under what conditions the WKB method is accurate enough to capture the carrier transport behavior is still unknown since the WKB method is an approximation method.[27] In this paper, another simulation method for the device with the coexistence of quantum transport and diffusive transport based on the NEGF method and the drift-diffusion simulation method is proposed. Since the NEGF method is more accurate but more time-consuming than the WKB method, the two methods are then further compared, and applicable conditions of the two simulation schemes are discussed to balance accuracy and computation cost.

The manuscript is organized as follows. In Sec. II, carrier transport simulation methods for electronic devices with the coexistence of quantum transport and drift-diffusion transport are presented. The verification of the simulation method is presented in Sec. III. In Sec. IV, a comprehensive study of the two carrier transport simulation methods is performed to explore their applicable condition, and the difference between the two current continuity conditions is compared and analyzed. The conclusions are finally drawn in Sec. V.

TABLE I. Simulation strategy: devices with coexistence of quantum transport and diffusive transport.

Step 1: Start with initial potential guess and initial quasi-Fermi level guess for the whole device;
Step 2: Calculate quantum transport current J_{QT} for quantum transport region by NEGF method or WKB method;
Step 3: Self-consistently solve drift-diffusion equations and Poisson's equation with current continuity condition, which is developed based on the quantum transport current calculated from step 2 (two methods to guarantee the current continuity are proposed and introduced in more detail in Sec. II D);
Step 4: **if** quantum transport current density is not converged $|(J_{QT} - J_{QT\text{-}old})/J_{QT\text{-}old}| >$ error
Go step 2;
else:
end;

II. MODELING AND SIMULATION METHODS

The simulation strategy is shown in Table I. The quantum transport simulation by NEGF or WKB methods is presented in more detail in Secs. II A and II B, respectively; the drift-diffusion simulation method is discussed in Sec. II A; and the current continuity conditions between quantum transport and diffusive transport are investigated in Sec. II D.

The shortened name of carrier transport simulation methods and current continuity conditions between quantum transport and drift-diffusion transport used in this paper are listed in Table II.

A. Quantum transport simulation by NEGF method

The NEGF method is briefly introduced in this subsection, and more details can be found in Refs. 28 and 29. The quantum

TABLE II. Shortened name of carrier transport simulation methods and current continuity conditions between quantum transport and drift-diffusion transport.

Shortened name	Methods
Carrier transport simulation method I	Combine NEGF method with drift-diffusion transport simulation method
Carrier transport simulation method II	Combine WKB method with drift-diffusion transport method
Current continuity condition I	Set the quantum transport current as connection boundary condition of drift-diffusion simulation
Current continuity condition II	Quantum transport current is transformed into carrier generation rates which is introduced into drift-diffusion equation

transport current can be calculated as[29]

$$J = -\frac{2q}{h}\int_{-\infty}^{+\infty} dE(\mathrm{Trace}[\Gamma_i A]f_i - \mathrm{Trace}[\Gamma_i G^n]), \quad (1)$$

where i is the terminal index, Γ is the broadening matrix, A is the spectral function, G^n is the electron correlation function, which can be calculated as $G^n = G\sum^{in} G^\dagger$.

Green's function is given as[28]

$$G(E) = \frac{1}{EI - H - \sum_1 - \sum_2}, \quad (2)$$

where H is the Hamiltonian, I is the identity matrix, and $\Sigma_{1(2)}$ is the self-energy matrix.

B. Quantum transport simulation by WKB approximation method

The quantum transport current calculated by the WKB method can be written as[27]

$$J = \frac{2q}{h}\int_{-\infty}^{+\infty} TC(E)(f(E - E_{FL}) - f(E - E_{FR}))dE, \quad (3)$$

where h is Planck's constant, E is the energy level, q is the elementary charge, and f is the Fermi function. E_{FL} and E_{FR} are the quasi-Fermi levels at the left and right ends of the quantum transport region, respectively. $TC(E)$ is the transmission coefficient and can be calculated as[27]

$$TC(E) = \exp\left(-\frac{2}{\hbar}\int_0^d \sqrt{2m_{\mathrm{diel}}(q\Phi_B - qF_{\mathrm{diel}}x - E)}dx\right), \quad (4)$$

where $\hbar$ is the reduced Planck constant, m_{diel} is the carrier effective mass, Φ_B denotes the left barrier height, F_{diel} is the electric field, and d is the thickness of the barrier.

C. Simulation methods in drift-diffusion transport region

The drift-diffusion equations and current continuity equations can be discretized by the Scharfetter–Gummel method and solved with Poisson's equation using the finite element method; more details can be found in Refs. 30 and 31.

D. Current continuity conditions between quantum transport and drift-diffusion transport

In this subsection, two methods are proposed to guarantee current continuity between quantum transport and drift-diffusion transport. The current continuity condition I: The quantum transport current is first calculated, which is set as the connection boundary condition for diffusive transport at the interface between the quantum transport region and drift-diffusion region.

The current continuity condition II: The quantum transport current is first calculated and transformed into a carrier generation rate, and then, the carrier generation rate is introduced to the drift-diffusion equations for the two diffusive transport regions, which sandwich the quantum transport regions. However, the generation rates in the two diffusive transport regions are with different signs: One is positive and the other is negative. The positive generation rate represents the carrier injection into the drift-diffusion transport region, and the negative generation term represents the carrier extraction from the drift-diffusion transport region.

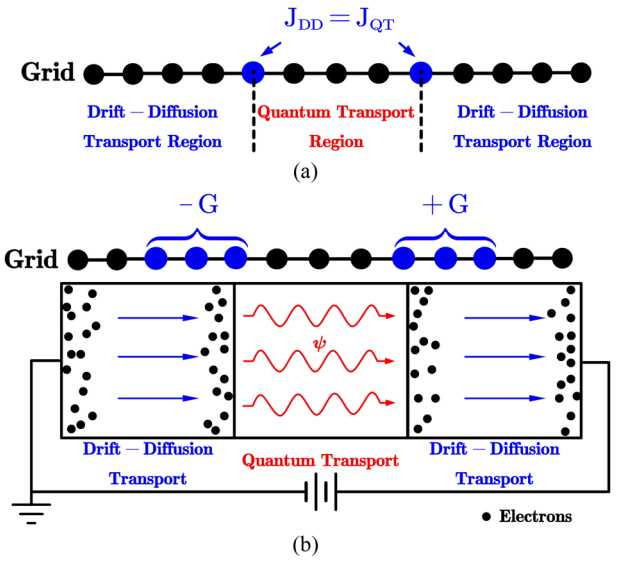

FIG. 2. (a) Schematic of current continuity condition I: The current in quantum transport region is first calculated by NEGF or WKB methods and set as the connection boundary condition of drift-diffusion transport simulation. (b) Schematic of current continuity condition II: The current in the quantum transport region is first calculated by the NEGF or WKB method and transformed into a positive and a negative carrier generation rate. The positive generation rate represents the carrier injection into the drift-diffusion transport region, and the negative generation term represents carrier extraction from the drift-diffusion transport region.

Taking electrons transporting from left to right as an example as illustrated in Fig. 2(b), hole transport can be treated similarly, and the quantum transport-induced carrier generation rates on the left and right sides of quantum transport region are positive and negative, respectively, and can be written as

$$G = \frac{J_{QTn}}{q\Delta L}, \quad (5)$$

where J_{QTn} is the electron current in the quantum transport region and the quantum transport-induced carrier generation rates are uniformly distributed over a length of ΔL, whose value can be set according to mean free path, diffusion length, energy relaxation length, or momentum relaxation length,[32–34] which can provide more flexibility to adapt the simulation results to measurements.

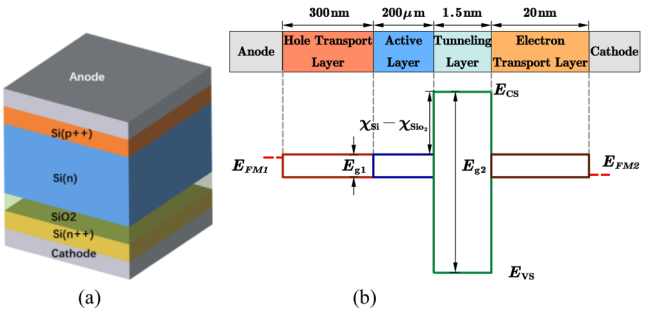

FIG. 3. (a) Structure and (b) flatband diagram of the n-type TOPCon solar cell based on the anode/hole transport layer (HTL)/active layer (AL)/tunnel layer (TL)/electron transport layer (ETL)/cathode stacks.[35] E_{g1} and E_{g2} represent the bandgap of Si and SiO_2, respectively, and χ_{Si} and χ_{SiO2} represent the electron affinity of Si and SiO_2, respectively. E_{CS}, E_{VS}, E_{FM1}, and E_{FM2} represent the conduction band edge, the valence band edge, the anode work function, and the cathode work function, respectively.

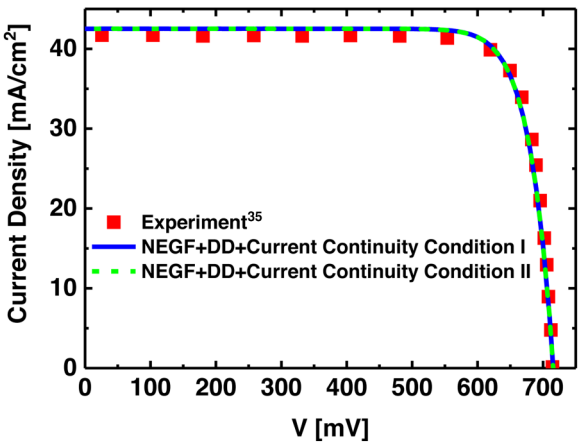

FIG. 4. Comparison of *J–V* curves calculated by our carrier transport simulation methods with the two current continuity conditions between the previous experimental result for the device with 1.5 nm oxide thickness.[35]

III. VERIFICATION OF SIMULATION METHODS

The correctness of the simulation method that combines NEGF with the drift-diffusion simulation method should be verified first before further investigation; hence, in this section, the n-type TOPCon solar cell is chosen as the simulation example and the *J–V* curves simulated using our methods are compared to the previous experimental results. The structure and the flatband diagram of the n-type TOPCon solar cell based on the anode/hole transport layer (HTL)/active layer (AL)/tunnel layer (TL)/electron transport layer (ETL)/cathode stacks are shown in Figs. 3(a) and 3(b), respectively. SiO_2 is treated as the quantum transport region in simulation since electrons can transport through it as waves, while Si is treated as the drift-diffusion transport region.

The *J–V* curves calculated by our carrier transport simulation methods under the two current continuity conditions are shown and compared with experimental results in Fig. 4, and the material parameters used in simulation are listed in Table III. For current continuity condition II as in Sec. II, ΔL is set as 10 nm. The acceptor doping concentration of the hole transport layer is $6 \times 10^{25}/m^3$, the donor doping concentration of the electron transport layer is $5 \times 10^{25}/m^3$, and the donor doping concentration of the active layer is $5 \times 10^{21}/m^3$. The electron mobility is 1400 $cm^2/V/s$, and the hole mobility is 450 $cm^2/V/s$. The electron effective mass in oxide is 0.30 m_0,[36] the electron affinity of SiO_2 is 0.95 eV,[36] and the thickness of SiO_2 is 1.5 nm.[35] Good agreements with the experimental results[35] are achieved.

IV. SIMULATION RESULTS AND DISCUSSION

In this section, the applicable conditions of the two carrier transport simulation methods are further explored for n-type TOPCon solar cells with different oxide thicknesses T_{ox}, different oxide barrier heights Φ_B ($=\chi_{ox} - \chi_{Si}$), which is adjusted by changing the electron affinity of oxide, different electron effective masses in oxide m_{ox}, and different doping concentrations in electron transport layer $N_{d,ETL}$. In addition, the differences in the *J–V* curves, carrier densities, and Shockley–Read–Hall (SRH) recombination rates simulated by method I under the two current continuity conditions separately for the device with different carrier mobilities are also explored and analyzed. The relative difference between the current densities simulated by methods I and II is defined as $|\Delta J/J| = |(J_1 - J_2)/J_1|$. Tight-binding Hamiltonian is used for the NEGF simulation.

Figure 5 shows the *J–V* curves calculated by the two carrier transport simulation methods with different oxide thicknesses (1.6, 1.8, and 2.0 nm). As the oxide thickness increases, the barrier width increases, which makes it harder for electrons to tunnel through and leads to a decrease in the current density. To explore the difference between the current densities calculated by the two carrier transport simulation methods, the comparisons of the band profile, transmission coefficient, and spectral current density calculated by the two methods are shown in Figs. 6(a)–6(c), respectively, and the coordinate of the left end of the oxide layer is set to 0.

Figure 6(b) shows the transmission coefficients calculated by NEGF or WKB methods for the solar cell with 1.8 nm oxide thickness and 600 mV voltage applied to the anode. The transmission coefficient calculated by the NEGF method is $TC(E) = \mathrm{Trace}(\Gamma_1 G \Gamma_2 G^\dagger)$. The reason for the difference between current

TABLE III. Material parameters of the n-type TOPCon solar cell.

Symbol	Quantity	Si	SiO_2
E_g	Bandgap	1.12 eV[36]	8.9 eV[36]
X	Electron affinity	4.05 eV[36]	…
ε_r	Relative permittivity	11.9[36]	3.9[36]
m_e	Electron effective mass	1.06 m_0[36]	…
m_h	Hole effective mass	0.59 m_0[36]	…

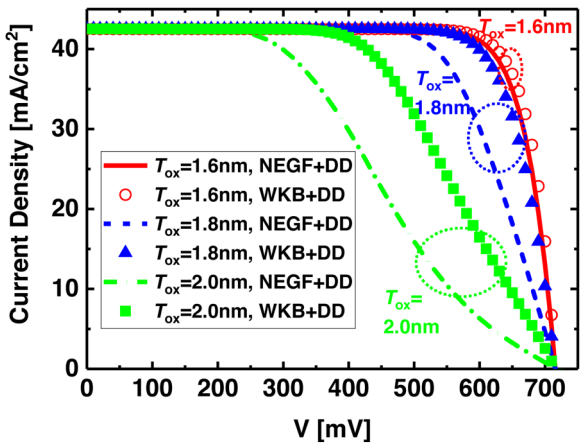

FIG. 5. *J–V* curves calculated by the two carrier transport simulation methods with different oxide thicknesses (1.6, 1.8, and 2 nm).

densities calculated by the two methods is that the transmission coefficient calculated by the NEGF method is smaller than that calculated by the WKB method for the energy level near the conduction band edge,[37] i.e., where the quantum transport current in the tunnel layer of the n-type TOPCon solar cell mainly comes from. Figure 6(c) shows the spectral current densities calculated by the two carrier transport simulation methods. For the energy level near the conduction band edge, the spectral current density calculated by the WKB method is larger than that calculated by the NEGF method, which further confirms our analysis.

The relationship between the relative difference in the current density and parameters corresponding to carrier tunneling in n-type TOPCon solar cells is given in Fig. 7 to explore the applicable conditions of the two carrier transport simulation methods. For the solar cell with oxide thickness thinner than 1.6 nm, oxide barrier lower than 3.3 eV, donor doping concentration greater than $1 \times 10^{25}\,m^{-3}$, and electron effective mass in oxide smaller than $0.35\,m_0$, the relative difference between current densities calculated by the two methods is approximately equal to zero; hence, method II is more suitable due to its low computational cost without loss of accuracy. As the oxide barrier width, barrier height, and electron effective mass increase, or the donor doping concentration in the electron transport layer decreases to the extent that the blocking effect of the oxide barrier on light-generated electrons becomes significant, method I is more accurate because the transmission coefficient for the energy level near the conduction band edge calculated by WKB is overestimated.

The reason why decreasing the donor doping concentration in the electron transport layer increases the current density relative difference is that the difference between the conduction band edge and quasi-Fermi level at the left and right ends of oxide is increased as shown in Fig. 7(c), which reduces the value of the Fermi function, thereby reducing the current density and also enhancing the blocking effect of the potential barrier on the light-generated electrons.

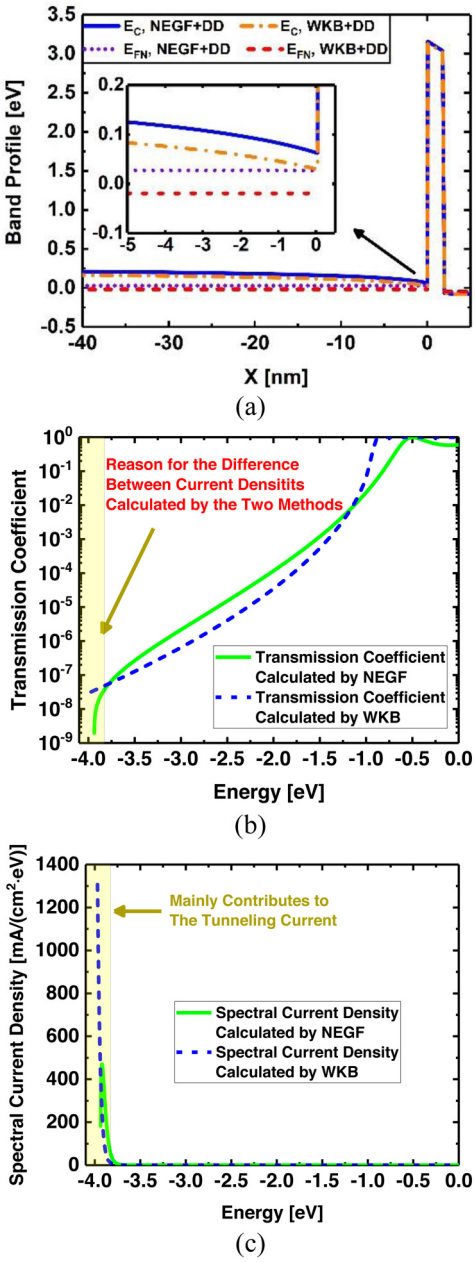

FIG. 6. (a) Comparison of band profiles calculated by the two carrier transport simulation methods for the device with 1.8 nm oxide thickness and 600 mV voltage applied to the anode. (b) Comparison of transmission coefficients calculated by NEGF or WKB methods for the device with 1.8 nm oxide thickness and 600 mV voltage applied to the anode. (c) Comparison of spectral current densities calculated by NEGF or WKB methods for the device with 1.8 nm oxide thickness and 600 mV voltage applied to the anode. The inset in (a) is the zoomed-in picture of the conduction band and electron quasi-Fermi level near the left end of the oxide simulated by the two methods, respectively. The energy levels that contribute the most to the quantum transport current are those covered by the yellow area in (b) and (c).

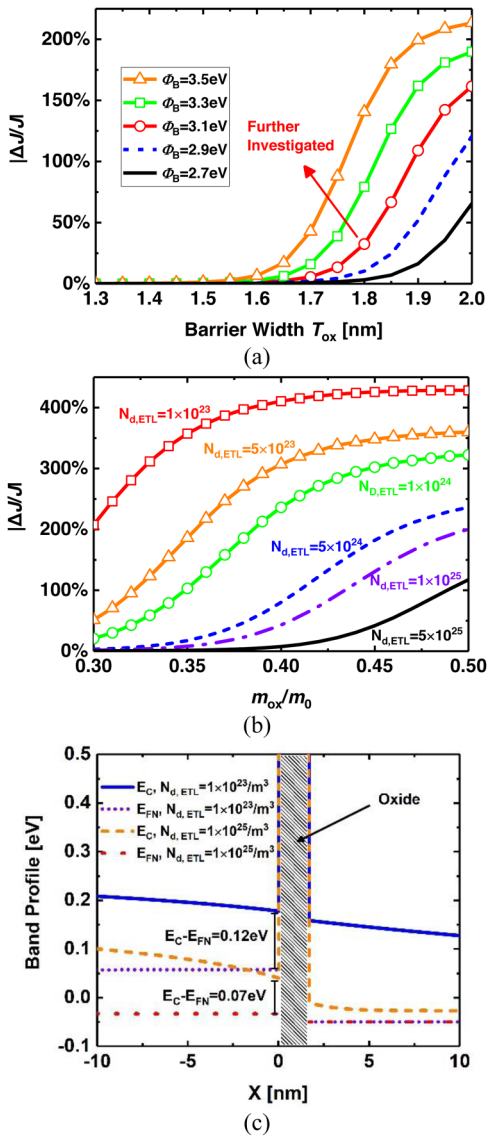

FIG. 7. (a) Relative difference between current densities calculated by the two methods as a function of oxide thickness for n-type TOPCon solar cells with different oxide barrier heights (Φ_B = 2.7, 2.9, 3.1, 3.3, and 3.5 eV). (b) The relative difference between current densities calculated by the two methods as a function of electron effective mass in oxide for n-type TOPCon solar cell with different donor doping concentrations in the electron transport layer ($N_{d,ETL}$ = 1 × 10^{23}, 5 × 10^{23}, 1 × 10^{24}, 5 × 10^{24}, 1 × 10^{25}, 5 × 10^{25} m^{-3}). (c) Band profile of the solar cell with 600 mV voltage applied to the anode calculated by the two carrier transport simulation methods with different doping concentrations in the electron transport layer ($N_{d,ETL}$ = 10^{23} and 10^{25}/m^3).

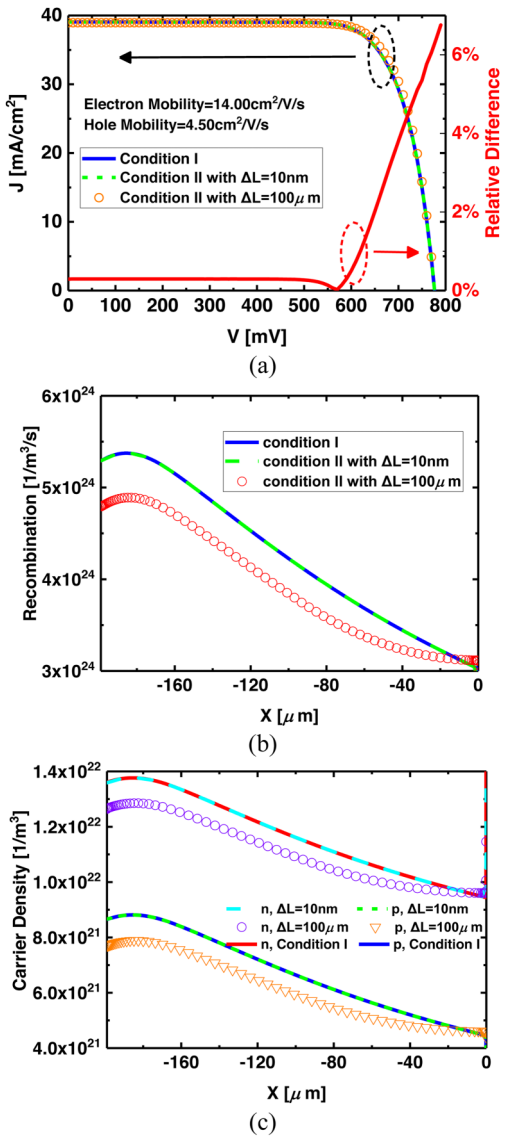

FIG. 8. (a) *J–V* curves calculated by carrier transport simulation method I under current continuity condition I and current continuity condition II with ΔL = 10 nm and ΔL = 100 μm, respectively, and the relative difference between current densities calculated under current continuity condition I and current continuity condition II with ΔL = 100 μm. (b) SRH recombination rates, and (c) carrier densities calculated by carrier transport simulation method I under current continuity condition I and current continuity condition II with ΔL = 10 nm and ΔL = 100 μm, respectively. The oxide thickness is 1.5 nm, the voltage applied to the anode is 700 mV, and the carrier mobility used in the simulation is scaled down by a factor of 100.

In addition, the differences in *J–V* curves, carrier densities, and SRH recombination rates calculated by carrier transport simulation method I under the two current continuity conditions separately are also further explored with different carrier lifetimes. The length of the quantum transport-induced carrier generation rate on the left side of the oxide is set to 10 and 100 μm, respectively, and the length of the quantum transport-induced carrier generation rate on the right side of the tunneling layer is set to 10 nm.

Figure 8(a) shows the J–V curves simulated using method I under current continuity condition I or II, respectively, and relative difference between current densities calculated under current continuity condition I or condition II with $\Delta L = 100\,\mu$m; the carrier mobility is scaled down by a factor of 100. The current density simulated under current continuity condition I is identical to that simulated under current continuity condition II with $\Delta L = 10$ nm but slightly differs from the current density simulated under current continuity condition II with $\Delta L = 100\,\mu$m. The maximum difference in the current density simulated under current continuity condition I and current continuity condition II with $\Delta L = 100\,\mu$m, respectively, is approximately 7%.

Figure 8(b) shows the SRH recombination rates calculated by method I with the application of the two current continuity conditions for the device with 700 mV voltage applied to the anode. It can be concluded that the main cause of the difference in current densities simulated under current continuity condition I and current continuity condition II with $\Delta L = 100\,\mu$m, respectively, is the difference in SRH recombination rates, and this is because the difference in current densities simulated under condition I and condition II with $\Delta L = 100\,\mu$m, respectively, is roughly equal to the difference in the current density loss caused by SRH recombination shown in Fig. 8(b), and the former is 1.11 mA/cm^2 and the latter is 1.02 mA/cm^2.

The reason why applying current continuity condition II with $\Delta L = 100\,\mu$m results in a lower SRH recombination loss is that the distance for light-generated electrons to transport to the cathode is shortened, which reduces the carrier accumulation in the active layer and leads to a lower carrier density as shown in Fig. 8(c).

V. CONCLUSION

In this manuscript, carrier transport simulation methods are proposed for devices with the coexistence of quantum transport and diffusive transport by combining the nonequilibrium Green's function (NEGF) method with solving drift-diffusion transport equation. A comprehensive study of our method and the method combining the WKB approximation method with solving drift-diffusion transport equation is performed to investigate their applicable conditions and balance the accuracy and computational cost. As the oxide barrier width, barrier height, and electron effective mass increase or the doping concentration in the electron transport layer decreases to the extent that the blocking effect of the oxide barrier on light-generated electrons cannot be ignored, method I is more accurate because the transmission coefficient near the conduction band edge calculated by WKB is overestimated; otherwise, method II is more suitable because its low computational cost without loss of accuracy. In addition, the differences in current densities, carrier densities, and SRH recombination rates simulated with the application of the two current continuity conditions separately with different carrier lifetimes are also further explored and analyzed.

ACKNOWLEDGMENTS

This work was supported by the National Natural Science Foundation of China (NSFC) under Grant Nos. 62122067 and U23A20351; in part, by the Zhejiang Provincial Natural Science Foundation under Grant Nos. LDT23F0402, LR21F010003, and LDT23F04021F04; in part by the Key Research and Development Program of Ningbo City under Grant No. 2023Z071; and in part by the Scientific Research Project of China Three Gorges Corporation under Grant No. 202203092.

AUTHOR DECLARATIONS

Conflict of Interest

The authors have no conflicts to disclose.

Author Contributions

Liang Tian: Conceptualization (equal); Data curation (equal); Formal analysis (equal); Investigation (equal); Methodology (equal); Resources (equal); Validation (equal); Visualization (equal). **Wei E. I. Sha:** Funding acquisition (supporting); Project administration (supporting); Writing – original draft (supporting); Writing – review & editing (supporting). **Hao Xie:** Writing – original draft (supporting); Writing – review & editing (supporting). **Dongxue Liu:** Funding acquisition (supporting). **Tian-Ge Sun:** Funding acquisition (supporting). **Yin-Shui Xia:** Writing – original draft (supporting); Writing – review & editing (supporting). **Wenchao Chen:** Funding acquisition (supporting); Project administration (lead); Supervision (lead); Validation (supporting); Writing – original draft (supporting); Writing – review & editing (supporting).

DATA AVAILABILITY

The data that support the findings of this study are available from the corresponding authors upon reasonable request.

REFERENCES

[1]D. Chen, Y. Chen, Z. Wang, J. Gong, C. Liu, Y. Zou, Y. He, Y. Wang, L. Yuan, and W. Lin, Sol. Energy Mater. Sol. Cells **206**, 110258 (2020).
[2]T. Gao, Q. Yang, X. Guo, Y. Huang, Z. Zhang, Z. Wang, M. Liao, C. Shou, Y. Zeng, and B. Yan, Sol. Energy Mater. Sol. Cells **200**, 109926 (2019).
[3]T. Yu, F. Wang, Y. Xu, L. Ma, X. Pi, and D. Yang, Adv. Mater. **28**(24), 4912–4919 (2016).
[4]R. M. France, J. F. Geisz, T. Song, W. Olavarria, M. Young, A. Kibbler, and M. A. Steiner, Joule **6**(5), 1121–1135 (2022).
[5]I. Sayed and S. M. Bedair, IEEE J. Photovoltaics **9**(2), 402–423 (2019).
[6]J. A. Gil-Corrales, J. A. Vinasco, M. E. Mora-Ramos, A. L. Morales, and C. A. Duque, Nanomaterials **12**(10), 1714 (2022).
[7]J. Wang, M. Naftaly, and E. Wasige, Appl. Sci. **12**(8), 3822 (2022).
[8]S. Suzuki, in *2022 International Electron Devices Meeting (IEDM)* (IEEE, 2022).
[9]A. D. Franklin, M. Luisier, S.-J. Han, G. Tulevski, C. M. Breslin, L. Gignac, M. S. Lundstrom, and W. Haensch, Nano Lett. **12**(2), 758–762 (2012).
[10]C. Y. Chen, H. Ilatikhameneh, J. Z. Huang, G. Klimeck, and M. Povolotskyi, IEEE Trans. Electron Devices **67**(8), 3478–3485 (2020).
[11]Y. Guan, V. P. Georgiev, A. Asenov, F. Liang, and H. Chen, IEEE Trans. Electron Devices **69**(11), 6394–6399 (2022).
[12]A. Rahman, G. Jing, S. Datta, and M. S. Lundstrom, IEEE Trans. Electron Devices **50**(9), 1853–1864 (2003).
[13]D. Nagy, A. Rezaei, N. Xeni, T. Dutta, F. Adamu-Lema, I. Topaloglu, V. P. Georgiev, and A. Asenov, Solid-State Electron. **199**, 108489 (2023).
[14]P. H. Ahn and S. M. Hong, IEEE Trans. Electron Devices **70**(1), 239–246 (2023).

[15]N. Sano, K. Yoshida, K. Tsukahara, and G. Park, IEEE Trans. Electron Devices **67**(8), 3323–3328 (2020).
[16]A. Singh and A. Gagliardi, Solar Energy **187**, 39–46 (2019).
[17]K. Takahashi, H. Tanaka, M. Kaneko, and T. Kimoto, IEEE Trans. Electron Devices **69**(4), 1989–1994 (2022).
[18]X. D. Wang, W. D. Hu, X. S. Chen, and W. Lu, IEEE Trans. Electron Devices **59**(5), 1393–1401 (2012).
[19]A. Saadat, M. L. Van de Put, H. Edwards, and W. G. Vandenberghe, IEEE Trans. Electron Devices **67**(11), 4990–4997 (2020).
[20]M. Ancona, COMPEL **6**(1), 11–18 (1987).
[21]M. Ancona and G. Iafrate, Phys. Rev. B **39**(13), 9536 (1989).
[22]M. Ieong, P. M. Solomon, S. Laux, H.-S. Wong, and D. Chidambarrao, in *International Electron Devices Meeting 1998. Technical Digest (Cat. No. 98CH36217)* (IEEE, 1998).
[23]W. Chen, A. Rinzler, and J. Guo, J. Appl. Phys. **113**(9), 094507 (2013).
[24]P. Chang, G. Du, J. Kang, and X. Liu, IEEE Electron Device Lett. **42**(1), 118–121 (2021).
[25]P. Procel, P. Löper, F. Crupi, C. Ballif, and A. Ingenito, Sol. Energy Mater. Sol. Cells **200**, 109937 (2019).
[26]L. De Michielis, N. Dağtekin, A. Biswas, L. Lattanzio, L. Selmi, M. Luisier, H. Riel, and A. M. Ionescu, Appl. Phys. Lett. **103**(12), 123509 (2013).
[27]A. Gehring, Simulation of Tunneling in Semiconductor Devices (Technischen Universität Wien, 2003).
[28]S. Datta, *Quantum Transport: Atom to Transistor* (Cambridge University Press, 2005).
[29]M. P. Anantram, M. S. Lundstrom, and D. E. Nikonov, Proc. IEEE **96**(9), 1511–1550 (2008).
[30]W. Chen, M. Wang, X. Yang, W. Y. Yin, and E. Li, in *2017 IEEE Electrical Design of Advanced Packaging and Systems Symposium (EDAPS)* (IEEE, 2017).
[31]Y. Taur and T. H. Ning, *Fundamentals of Modern VLSI Devices* (Cambridge University Press, 2021).
[32]E. H. Sondheimer, Adv. Phys. **50**(6), 499–537 (2001).
[33]T. Tomita, Y. Kamakura, and K. Taniguchi, Phys. Status Solidi B **204**(1), 129–132 (1997).
[34]E. Gnani, A. Gnudi, S. Reggiani, and G. Baccarani, IEEE Trans. Electron Devices **57**(1), 336–344 (2010).
[35]H. Steinkemper, F. Feldmann, M. Bivour, and M. Hermle, IEEE J. Photovoltaics **5**(5), 1348–1356 (2015).
[36]S. Kar, *High Permittivity Gate Dielectric Materials* (Springer, 2013).
[37]A. Kloes, M. Schwarz, Y. Han, Q. T. Zhao, and C. Roemer, in *2023 30th International Conference on Mixed Design of Integrated Circuits and System (MIXDES)* (IEEE, 2023).